Single-point structure tensors in rough-wall turbulent channel flow

By J. Yuan, G. Brereton†, G. Iaccarino, A. A. Mishra AND M. Vartdal ‡

A long-standing problem in turbulence modeling is that the Reynolds stress tensor alone is not necessarily sufficient to characterize the transient and non-equilibrium behaviors of turbulence under arbitrary mean deformation or frame rotation. More complete flow characterizations include additional, single-point structure tensors, such as the dimensionality, circulicity and inhomogeneity tensors. These tensors are one-point correlations of local stream-vector gradients and can carry some non-local information on structure. We explore the role of these tensors in smooth- and rough-wall channel flows using existing DNS data, to improve understanding and modeling of these complex flows. To account for the immersed boundary method used in the rough-wall DNS, an immersed boundary method for the stream-vector Poisson equation is developed in the framework of Stylianou *et al.* (2015). Results show that the roughness effects on the inclination and aspect ratio of two-point velocity correlation inside the roughness sublayer are qualitatively reproduced by their corresponding single-point tensor representations; in the outer layer, quantitative agreement is obtained. Other observations on structural change of turbulence on account of wall roughness and their relevance to turbulence modeling are discussed.

1. Introduction

A wide range of wall-bounded turbulent flows in engineering and environmental applications are characterized by high Reynolds numbers and surface roughness. Their dynamics are further complicated by additional factors such as pressure gradients, unsteadiness, surface curvature, complex geometries, etc. At present and in the foreseeable future, the only pragmatic computational approach to simulate such non-equilibrium turbulent boundary layers is to use single-point closures in the vicinity of the wall or throughout the boundary layer.

The ability of single-point closures to model different features of turbulent flows is encumbered by the fact that the state of the turbulent flow field has to be expressed using only the Reynolds stresses. This corresponds to a coarse-grained description of the turbulent flow field and limits the features of turbulence that such models can potentially replicate. For instance, Sagaut & Cambon (2008) have shown that in the presence of background rotation, Reynolds stress anisotropy should be decomposed into directional and polarization anisotropy, each of which is oppositely affected by the pressure-velocity correlations through the action of the Coriolis force. This coarse grained description introduces uncertainty in the modeling problem (Mishra *et al.* 2016) as all turbulent flows with the same Reynolds stress need not evolve identically under the same conditions. Kassinos and co-workers (Kassinos & Reynolds 1994) have shown that using just the

† Department of Mechanical Engineering, Michigan State University
‡ Norwegian Defence Research Establishment (FFI)

Surface	Re_τ	k_s^+	k_c/δ	$(L_x, L_z)/\delta$	(n_i, n_j, n_k)	$(\Delta x^+, \Delta y^+_{\text{min}}, \Delta z^+)$
Smooth	1000	–	–	$(6, 3)$	$(512, 256, 512)$	$(11.7, 0.3, 5.8)$
Sand-grain roughness	1000	78	0.09	$(6, 3)$	$(1024, 236, 512)$	$(6.0, 0.7, 6.0)$

TABLE 1. Open-channel DNS data summary. Superscript "+" indicates normalization in wall units. L_x, L_z are domain sizes. δ is channel half-height. k_c is roughness crest height.

Reynolds stresses to characterize the turbulent flow field limits the models by eschewing information regarding dynamically important physics. The Reynolds stresses only carry information regarding the componentality of turbulence, or the relative strengths of different velocity components. Kassinos *et al.* (2001) introduced additional tensors to the modeling basis that add important information, such as the structure dimensionality tensor, which characterizes the relative uniformity of the turbulence structure in different directions. This improves turbulence model predictions in homogeneous turbulent flows. The aforementioned effects of coarse-graining are exacerbated for inhomogeneous turbulent flows, such as regions in the vicinity of a wall.

To explore the capability of these structure tensors in modeling inhomogeneous flows, it is important to clarify whether they still represent similar information as they do for a homogeneous flow. For example, it can be shown (Bhattacharya *et al.* 2008) that the dimensionality tensor represents the characteristics of the two-point velocity correlation. Specifically, the tensor eigenvalue ratio represent the aspect ratio of the contour and the tensor principle axes inclination represents the contour rotation. This is true, however, under the assumptions of homogeneous turbulence in the inertial subrange. It is not clear whether such representations still apply near the wall, where turbulence is inhomogeneous and the local Reynolds number is limited.

In this work, we explore the structure representation for wall turbulence above smooth and rough walls. The structural characteristics are compared with what the structure tensors would indicate as in the case of a homogeneous turbulence; we explore whether these tensors capture near-wall structural change due to roughness. DNS data of open-channel flows over a smooth wall and a synthetic sand-grain roughness are used; the simulations are described in Yuan & Piomelli (2014). Section 2 summarizes the simulation parameters and provides details of calculations of the stream vector and the single-point tensors. These calculations are validated in Section 3. Section 4 compares characteristics of the actual structure and the tensors. Section 5 boils down the tensors to their principle information that can be used for modeling purposes. Insights are provided on turbulence closure developments.

2. Problem formulation and methodologies

2.1. *Simulation data*

The parameters of the DNS simulations are summarized in Table 1. Here, x_1, x_2 and x_3 (or x, y and z) are, respectively, the streamwise, wall-normal and spanwise directions, and u_j (or u, v and w) are the velocity components in those directions. For the rough case, an immersed boundary method based on the volume-of-fluid approach is used to impose no-slip boundary conditions on the rough surface. The simulations are performed using a well-validated code that solves the governing equations on a staggered grid using second-order, central differences for all terms, second-order accurate Adams-Bashforth semi-implicit time advancement, and MPI parallelization.

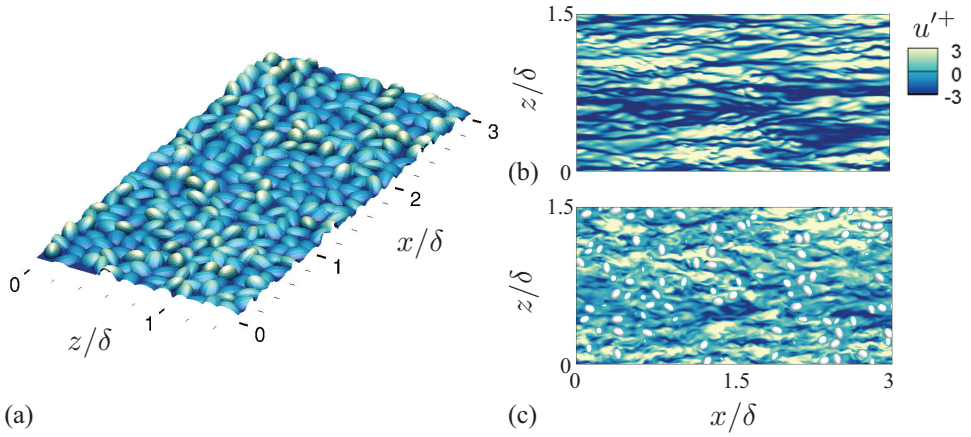

FIGURE 1. (a) One fourth of sand-grain rough surface colored by height. Instantaneous contours of u'^+ (b) at $y^+ = 10$ on smooth wall and (b) at $y/d = 1$ on rough wall. d is the virtual origin, obtained as the apparent location of rough-wall drag (Jackson 1981).

The synthetic rough surface is shown in Figure 1(a). It consists of randomly rotated and distributed ellipsoids. The grain shape is well resolved by around 20 grid points per direction. The roughness Reynolds number k_s^+ is 80, ensuring that the flow is in the fully rough regime. The crest height $k_c = 0.09\delta$; Townsend's similarity hypothesis is expected for second-order statistics as observed previously in Yuan & Piomelli (2014). Figure 1(b-c) compare instantaneous u'^+ in the smooth-wall buffer layer and in the roughness sublayer, showing a clear structural change associated with the break-up of low-speed streaks.

In the roughness sublayer, roughness leads to spatial heterogeneity of a time-averaged variable; such time-averaged perturbations in space are separated from the turbulent fluctuations using the double-averaging decomposition introduced by Raupach & Shaw (1982),

$$\theta(\boldsymbol{x}, t) = \langle\overline{\theta}\rangle(y) + \widetilde{\theta}(\boldsymbol{x}) + \theta'(\boldsymbol{x}, t), \tag{2.1}$$

where θ is an instantaneous flow variable, $\langle\theta\rangle$ is the intrinsic spatial average in the (x, z)-plane, $\langle\theta\rangle = 1/A_f \int_{A_f} \theta dA$ (where A_f is the area occupied by fluid), $\overline{\theta}$ is the temporal average, $\theta' = \theta - \overline{\theta}$ is the instantaneous turbulent fluctuation, and $\widetilde{\theta} = \overline{\theta} - \langle\overline{\theta}\rangle$ is the form-induced fluctuation.

2.2. *Structure-tensor calculation*

2.2.1. *Smooth-wall open channel*

The structure tensors are second-order moments of the 3D instantaneous stream vector, $\boldsymbol{\psi}$, which is determined from a Poisson equation,

$$-\boldsymbol{\nabla}^2\boldsymbol{\psi} = \boldsymbol{\omega}, \tag{2.2}$$

where $\boldsymbol{\omega}$ is the vorticity vector. $\boldsymbol{\psi}$ relates to $\boldsymbol{u}$ through $u_i = \epsilon_{ijk}\psi_{k,j}$, where ϵ_{ijk} is the Levi-Civita symbol.

The boundary conditions of Eq. (2.2) can be imposed as (Stylianou *et al.* 2015)

$$n_\alpha\psi_\alpha + n_\beta\psi_\beta + n_\gamma\psi_\gamma = 0, \tag{2.3}$$

$$-n_\alpha\frac{\partial\psi_\beta}{\partial x_\alpha} - n_\gamma\frac{\partial\psi_\beta}{\partial x_\gamma} = -n_\alpha\frac{\partial\psi_\alpha}{\partial x_\beta} - n_\gamma\frac{\partial\psi_\gamma}{\partial x_\beta} + \epsilon_{\beta jk}n_j u_k, \tag{2.4}$$

$$-n_\alpha \frac{\partial \psi_\gamma}{\partial x_\alpha} - n_\beta \frac{\partial \psi_\gamma}{\partial x_\beta} = -n_\alpha \frac{\partial \psi_\alpha}{\partial x_\gamma} - n_\beta \frac{\partial \psi_\beta}{\partial x_\gamma} + \epsilon_{\gamma jk} n_j u_k, \tag{2.5}$$

where n_α is the projection of the unit normal vector (pointing out of the boundary) in the dominant direction; n_β, n_γ are the other two components that, together with n_α, comply with the right hand rule.

The single-point structure tensors include the Reynolds stress (R), dimensionality (D), circulicity (F) and inhomogeneity tensors (C). They are defined according to Kassinos *et al.* (2001) as

$$R_{ij} = \epsilon_{ijk}\epsilon_{jki}\overline{\psi'_{k,j}\psi'_{i,k}},\ D_{ij} = \overline{\psi'_{k,i}\psi'_{k,j}},\ F_{ij} = \overline{\psi'_{i,k}\psi'_{j,k}},\ C_{ij} = \overline{\psi'_{i,k}\psi'_{k,j}}. \tag{2.6}$$

Following Stylianou *et al.* (2016), we calculate R, D, and F through an alternative approach based on a third-rand tensor, Q,

$$R_{ij} = \epsilon_{imp}Q_{mjp},\ D_{ij} = \epsilon_{imp}Q_{pmj} + C_{ij},\ F_{ij} = \epsilon_{imp}Q_{jpm} + C_{ji}, \tag{2.7}$$

where

$$Q_{ijk} = -\overline{u'_j\psi'_{i,k}}. \tag{2.8}$$

Compared to calculation through tensor definitions in Eq. (2.6), Eq. (2.7) has been shown to give less numerical error associated with the discretization of $\psi_{i,j}$ (Stylianou *et al.* 2016). The associated normalized form (r, d, f and c) is obtained through normalization with the respective trace values, except for c_{ij}, which is obtain by normalizing C_{ij} with D_{kk} instead of C_{kk}, since C_{ij} is not positive semi-definite.

Equation (2.2) is recast to a system of linear equations using second-order central difference (first-order one-sided difference at the domain boundaries) and is solved using a successive over-relaxation scheme. For the smooth-wall channel flow, the Poisson equations and the boundary conditions for the three ψ_i components are decoupled; ψ_i are solved successively. For the rough case, however, the immersed boundary implementation leads to coupling of the three ψ_i components; they are solved concurrently. Also note that, for the rough cases, $\langle\overline{(\cdot)}\rangle$ is used instead of $\overline{(\cdot)}$ for averaging in the tensor calculation.

2.2.2. *Immersed boundaries in stream-vector solver*

For the rough case, two types of ψ_i boundary conditions are imposed: (1) domain boundary conditions same as in the smooth channel and (2) immersed boundaries. Inside the immersed regions, the wall boundary condition (Eqs. (2.3)–(2.5)) is imposed with $\alpha = 2$, $\beta = 3$, $\gamma = 1$. These equations are rearranged as

$$\psi_2 = -\frac{n_3}{n_2}\psi_3 - \frac{n_1}{n_2}\psi_1, \tag{2.9}$$

$$\frac{\partial \psi_3}{\partial y} = -\frac{n_1}{n_2}\frac{\partial \psi_3}{\partial x} + \frac{\partial \psi_2}{\partial z} + \frac{n_1}{n_2}\frac{\partial \psi_1}{\partial z} - \frac{n_1}{n_2}v + u, \tag{2.10}$$

$$\frac{\partial \psi_1}{\partial y} = -\frac{n_3}{n_2}\frac{\partial \psi_1}{\partial z} + \frac{\partial \psi_2}{\partial x} + \frac{n_3}{n_2}\frac{\partial \psi_3}{\partial x} + \frac{n_3}{n_2}v - w. \tag{2.11}$$

These boundary conditions are equivalent to setting (1) zero wall-normal component of ψ at the immersed boundary and (2) constant tangential component of ψ across the immersed boundary.

Currently, no local ψ_i reconstruction is performed to ensure a sharp interface; future improvement is required for higher numerical accuracy. The local normal vector of the

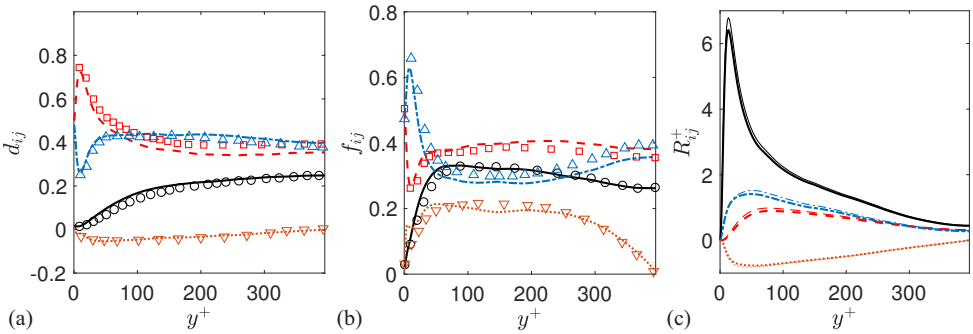

FIGURE 2. (a-b) Self-normalized tensors: present (lines) compared to Vartdal (2016) (symbols) for channel flow LES with $Re_\tau = 395$. (c) $\boldsymbol{R}$ from Eq. (2.8) (thick lines) versus error-free calculation (thin lines). 11 component: ——— , ◯; 22: – – – , □ ; 33: - - - , △; 12: - - - , ▽.

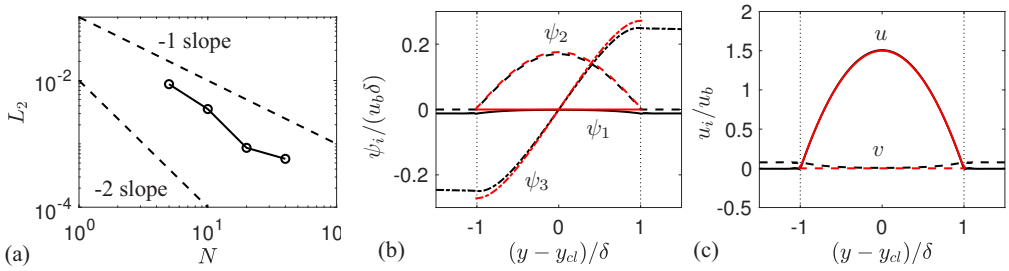

FIGURE 3. Validation of immersed boundary implementation using a tilted channel. (a) L_2-norm error of reconstructed u velocity versus the number of grid points spanning channel height, N. Comparison between (b) ψ_i and (c) reconstructed u_i for $N = 80$: immersed boundary implementation (black) versus calculation without immersed boundaries (red or grey). Normalization done with bulk velocity u_b and δ; y_{cl} is center-line elevation.

immersed boundary $\boldsymbol{n}$ for each (x, z) location (pointing from fluid to solid) is obtained from the roughness height distribution and is considered constant extending into the solid along y. To discretize Eqs. (2.9)-(2.11), central differences are used for the x and z derivatives, while first-order differences are used for y gradients. Second-order one-sided scheme may be used for y gradients to improve accuracy.

3. Code validation

To validate the stream-vector solver without immersed boundaries, $\boldsymbol{\psi}$ are calculated from LES data of a smooth-wall channel flow with $Re_\tau = 395$. The self-normalized tensors are compared with results obtained from a similar channel-flow simulation in Vartdal (2016) in Figure 2(a,b). Good collapse is obtained; the slight differences may be due to the fact that Vartdal (2016) calculated the tensors through their definitions, instead of Eq. (2.7). The Reynolds stress tensor obtained from Eq. (2.7) is compared to results from the alternative calculation $R_{ij} = \langle \overline{u_i' u_j'} \rangle$, which is free of error from the $\boldsymbol{\psi}$ solver; the discrepancy quantifies the numerical error of the tensor calculation of up to 3% of local R_{kk} value. For the DNS cases summarized in Table 1, such error is estimated as up to 7% of R_{kk}.

A laminar tilted channel simulation is used to test the implementation of immersed

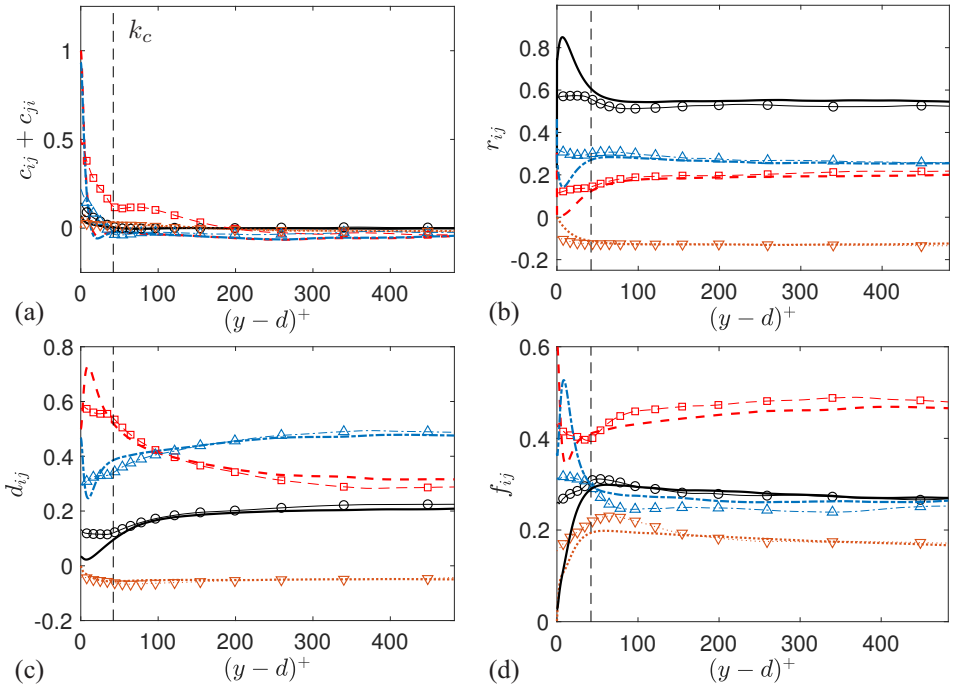

FIGURE 4. Self-normalized tensors for smooth (thick lines) and rough (thin lines and symbols) cases. 11 component: ——— , ◯; 22: – – – , □ ; 33: -·-·- , △; 12: ··· , ▽.

boundaries in the stream-vector solver. The channel is tilted in the (x, y) plane at an angle of 45° from the global coordinates with which the Cartesian grid aligns. Uniform grid is used in all directions. Results of ψ_i and the velocities reconstructed from ψ_i are compared in Figures 3(b,c) with their counterparts obtained from a same channel flow aligned with the coordinate (without immersed boundaries). Coordinate transform is performed to reorient ψ_i and u_i to the channel direction. Good collapse is obtained for all ψ_i and u_i components. Figures 3(a) shows that the L_2-norm error of the reconstructed u decreases with the number of grid points in a rate between first and second orders.

4. Results

Various normalized tensors are compared between the smooth and rough cases in Figure 4. Differences are confined in the near-wall region, supported by Townsend's similarity. Overall, roughness promotes the isotropy of $\boldsymbol{R}$, $\boldsymbol{D}$ and $\boldsymbol{F}$, as well as the near-wall magnitudes of their shear components.

First, the inhomogeneity tensor $\boldsymbol{C}$ becomes negligible in homogeneous turbulence. The extent of inhomogeneous turbulence from the wall has significance for modeling purposes, as only two tensors are sufficient to describe the state of the flow in homogenous turbulence; also, $R_{kk} = D_{kk} = F_{kk} = q^2$ (Kassinos *et al.* 2001), good news for turbulence modeling. Figure 4(a) shows that, on the smooth wall the strongly inhomogeneous region (with $c_{ij} + c_{ji}$ of order 1) extends to $y^+ \approx 10$. On rough wall this layer is confined to the region below the crest, k_c, due to the presence of rough surface below this elevation. For

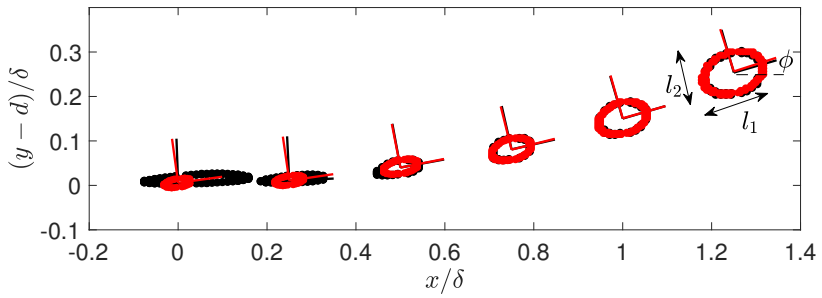

FIGURE 5. Trace of two-point velocity correlation tensor with contour level between 0.7 and 0.75 centered at various y locations for smooth (black) and rough (red or grey) cases. Short lines indicate principle axes of the contours. Contours are shifted in x for 0.25δ for clarity.

a limited region above k_c, the flow is weakly inhomogeneous; this is probably due to the small-scale form-induced shear, $\partial\widetilde{u}_i/\partial x_j$, inside the roughness sublayer.

The circulicity tensor $\boldsymbol{F}$ in Figure 4(d) characterizes the circulation of energy-containing motions. The dominance of 22 and 33 components near the smooth wall is due to $\partial u'/\partial y$ and $\partial u'/\partial z$ on account of low- and high-speed streaks (Stylianou *et al.* 2016). In addition, the rapid increase of 11 components from the smooth wall towards a peak at $y^+ \approx 30$ can be related to the quasi-streamwise vortices. On the rough wall, all normal components remain significant in the vicinity of the wall; this is consistent with the roughness-scale three-dimensional vortical structures such as the head-down and head-up hairpins (Talapatra & Katz 2012). The 22 component remains the strongest component throughout the boundary layer, probably due to the significant spanwise shear rates ($\partial u'/\partial z$) as a result of the alternating low and high momentum regions.

The dimensionality tensor $\boldsymbol{D}$ shown in Figure 4(c) characterizes the directional anisotropy of turbulence. A high value of its normal component represents shorter coherence in the corresponding direction. For homogeneous turbulence, it characterizes the coherent motions of scales in the inertial-subrange (Bhattacharya *et al.* 2008). It is shown that roughness weakens the streamwise elongation of structure (higher d_{11}), and the extents in z and y become similar, as the roughness elements impose their scales to the flow. Also, d_{12} shows higher magnitudes near the wall, indicating an increase of inclination angle of the tensor principle axes.

We now test whether the homogeneous-flow interpretation of $\boldsymbol{D}$ shown in Bhattacharya *et al.* (2008) still applies in the near-wall region with inhomogeneous turbulence and low local Reynolds numbers. Figure 5 compares the evolution of coherent structure along y using the isocontour of two-point velocity correlation tensor trace. At each elevation, the shape and inclination of the isocontour can be characterized by its aspect ratio, $AR = l_1/l_2$, and inclination angle, ϕ.

Figure 6 (a) compares ϕ and AR obtained from two-point velocity correlation with the corresponding tensor representations—the principle axes direction of $\boldsymbol{D}$ and its eigenvalue ratio, respectively. Contour-level ranges from 0.45 to 0.8 are used to show the general trend and the level of uncertainty based on the two-point correlation; the uncertainty for ϕ increases with y. Here, all ranges satisfy $r^+ > 12$ and $r/\delta \leq 0.25$ at all y locations calculated ($\boldsymbol{r}$ is the two-point separation in x or y) to exclude contribution from the dissipative and energy-containing ranges, where the tensor representations are known to fail. Far from the wall, the tensor predictions fall within the scatter of the actual structural

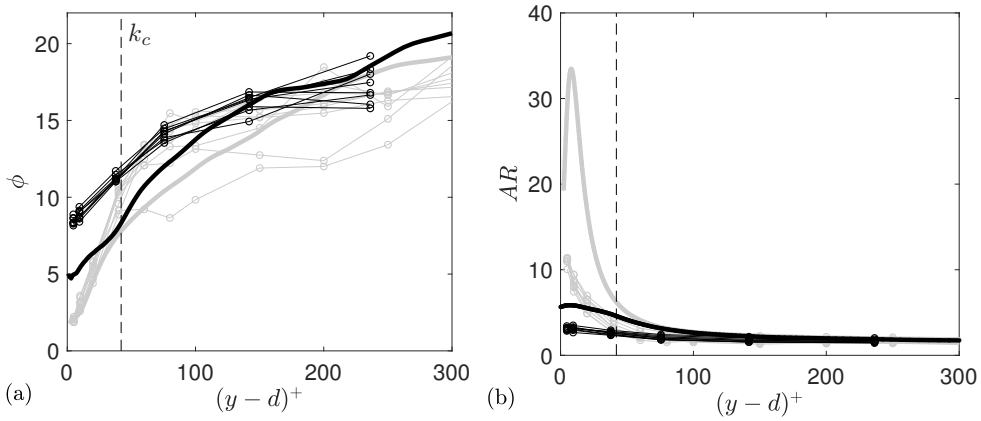

FIGURE 6. Actual structural properties (thin lines with symbol) versus tensor prediction (thick lines): (a) inclination angle (in degrees) and (b) aspect ratio of velocity-correlation isocontours with various contour-level ranges. Grey: smooth wall; black: rough wall.

properties for both cases. Good collapse is expected, as the relatively high local Reynolds number provides an inertial subrange and the flow is locally homogeneous. Near the wall, roughness leads to a clear increase of inclination angle and a reduced aspect ratio. The tensor representations capture these changes, qualitatively, though not quantitatively. This is due to the fact that, near the wall, there is no prominent inertial subrange, and turbulence is inhomogeneous.

5. Principle tensor information

The tensor components are not directly helpful for modeling purposes. This is because, even for structure-based closures such as the one of Kassinos *et al.* (2000), it is impractical to impose the boundary condition for each tensor component. Instead, one imposes the minimal amount of information that describes the structural changes from the wall to the outer layer, and from a smooth wall to a rough wall. One option is to break down the full tensors into (1) the principle-axes inclination angles and (2) the anisotropy invariants. Together with the tensor trace, these characteristics provide principle tensor information.

Figure 7(a) shows the principle-axes rotation for each tensor. Away from the smooth wall, the angles increases rapidly for all tensors; roughness leads to significantly high angles near the wall, tending to match the values above. The barycentric maps (Banerjee *et al.* 2007) in Figure 7(b-d) capture the anisotropy variation due to both elevation and surface roughness. On a smooth wall, R develops from quasi-one-component (1C) state, with most TKE residing in u'^2 associated with the low-speed streaks, to almost three-component (3C) above $y/\delta \approx 0.1$. D transitions from a two-component (2C) limit at the wall (due to structure elongation along x) to a near isotropic state. Similarly, F is 2C at the wall since the energy-containing streaky structure contributes mainly to circulations around y and z directions; away from the wall, F develops towards 3C state as the quasi-streamwise vortices contribute to streamwise circulation. In contrast, in the vicinity of the rough wall all tensors stay in a near 3C state. This can be explained through the established understanding that, inside the roughness sublayer, quasi-streamwise vortices coexist with roughness-scale eddies born from shear-layer roller-up, associated with the

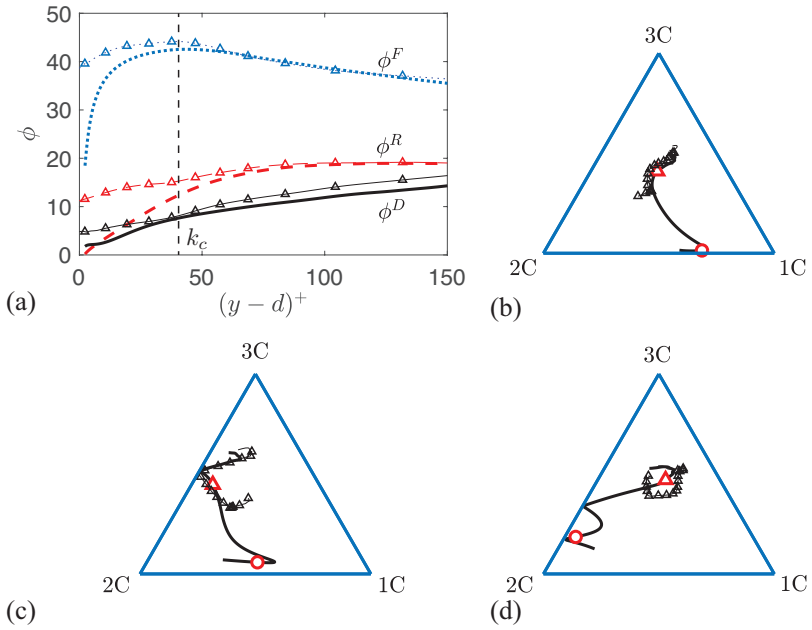

FIGURE 7. (a) Inclination angles (in degrees) of principle coordinates of D (———), R (- - -) and F (···) tensors for smooth (lines) and rough (△) cases. Barycentric maps showing the change of anisotropies of (b) R, (c) D and (d) F tensors in region $0 < (y-d)/\delta < 0.7$, for smooth (———) and rough (△) cases; large symbols: ◯ $y^+ = 5$, △ $y/\delta = 0.1$.

local wake regions. We show here that, for closure purposes, the roughness sublayer of a fully-rough flow can be considered structurally similar to the outer layer.

These results can be used to provide guidance on structure-based closures. For instance, Kassinos *et al.* (2000) proposed modeling the transport of Q for a homogeneous turbulence to emulate the effects of turbulence structure on non-equilibrium dynamics. The smooth-wall boundary condition was imposed by tuning the redistributive processes of Q-transport through an elliptic-relaxation approach. The results herein provide data for fine-tuning of such closure on smooth wall to match the main characteristics of various tensors, and for extending it to rough-wall flows, which would require a rather different boundary condition to yield a near isotropic state.

6. Conclusions

The single-point structure tensors have been show promising for physics-based turbulence closure as they are effective measures of non-local characteristics of homogeneous turbulence (Kassinos *et al.* 2000). In this work, we show that for inhomogeneous turbulence these tensors still contain qualitative information of the actual structure, and quantify their variations due to wall condition and elevation. An immersed-boundary approach is developed in the Poisson solver for the stream vector to extract these tensors on a complex rough surface. Results show that, in the roughness sublayer, the turbulence is weakly inhomogeneous. In this region, characteristics of the dimensionality tensor qualitatively capture the higher near-wall structure inclination angle on account of roughness,

as well as the shortening of streamwise coherence. In addition, the circulicity tensor becomes more isotropic, consistent with the emergence of roughness-scale vortical structure. Compared to a smooth-wall flow, on a rough wall turbulence appears structurally simpler, which is encouraging from a modeling standpoint. Overall tensor characteristics such as principle-axes inclination and anisotropy are shown to be sensitive to both roughness and elevation; thus, they may prove useful in a structure-based turbulence closure. Methodologies to impose rough-wall boundary conditions for such closures will be developed in future work.

Acknowledgments

The authors acknowledge use of computational resources from the Certainty cluster awarded by the National Science Foundation to CTR, and from Michigan State University's High Performance Computing Facility.

REFERENCES

Banerjee, S., Krahl, R., Durst, F. & Zenger, C. 2007 Presentation of anisotropy properties of turbulence, invariants versus eigenvalue approaches. *J. Turbul.* **8**, N32.

Bhattacharya, A., Kassinos, S. C. & Moser, R. D. 2008 Representing anisotropy of two-point second-order turbulence velocity correlations using structure tensors. *Phys. Fluids* **20**, 101502–1—13.

Jackson, P. S. 1981 On the displacement height in the logarithmic velocity profile. *J. Fluid Mech.* **111**, 15–25.

Kassinos, S. C., Langer, C. A., Haire, S. L. & Reynolds, W. C. 2000 Structure-based turbulence modeling for wall-bounded ows. *Int. J. Heat Fluid Flow* **21**, 599–605.

Kassinos, S. C. & Reynolds, W. C. 1994 A structure-based model for the rapid distortion of homogeneous turbulence. Report tf-61. Thermosciences Division, Department of Mechanical Engineering, Stanford University.

Kassinos, S. C., Reynolds, W. C. & Rogers, M. M. 2001 One-point turbulence structure tensors. *J. Fluid Mech.* **428**, 213–248.

Mishra, A. A., Iaccarino, G. & Duraisamy, K. 2016 Sensitivity of flow evolution on turbulence structure. *Phys. Rev. Fluids* **1** (5), 052402–1–11.

Raupach, M. R. & Shaw, R. H. 1982 Averaging procedures for flow within vegetation canopies. *Bound.-Lay. Meteorol.* **22**, 79–90.

Sagaut, P. & Cambon, C. 2008 *Homogeneous turbulence dynamics*, , vol. 10. Cambridge: Cambridge University Press.

Stylianou, F. S., Pecnik, R. & Kassinos, S. C. 2015 A general framework for computing the turbulence structure tensors. *Comput. Fluids* **106**, 54–66.

Stylianou, F. S., Pecnik, R. & Kassinos, S. C. 2016 Analyzing a turbulent pipe flow via the one-point structure tensors: Vorticity crawlers and streak shadows. *Comput. Fluids* **140**, 450–477.

Talapatra, S. & Katz, J. 2012 Coherent structures in the inner part of a rough-wall channel flow resolved using holographic PIV. *J. Fluid Mech.* **711**, 161–170.

Vartdal, M. 2016 Computing turbulence structure tensors in plane channel flow. *Comput. Fluids* **136**, 207–211.

Yuan, J. & Piomelli, U. 2014 Roughness effects on the reynolds stress budgets in near-wall turbulence. *J. Fluid Mech.* **760**, R1.